*AAPS PharmSciTech, Vol. 14, No. 1, March 2013 (© 2012)*
DOI: 10.1208/s12249-012-9890-4

*Research Article*

# Application of Near-Infrared Spectroscopy in Real-Time Monitoring of Product Attributes of Ribbed Roller Compacted Flakes

**Asim Kumar Samanta,[1] Atul D. Karande,[1] Ka Yun Ng,[1] and Paul Wan Sia Heng[1,2]**

*Received 28 July 2012; accepted 5 November 2012; published online 11 December 2012*

***Abstract.*** This study assessed the utility of near-infrared (NIR) spectroscopy for the real-time monitoring of content uniformity and critical quality attributes (tensile strength, Young's modulus, and relative density) of ribbed roller compacted flakes made by axially corrugated or ribbed rolls. A custom-built setup was used to capture off-line NIR spectra from the flakes containing micronized chlorpheniramine maleate, microcrystalline cellulose, lactose, and magnesium stearate. The partial least square regression method was employed to build calibration models from these off-line NIR spectra using experimental design and validated using test set validation. During calibration model development, various factors, such as spectral acquisition mode, probe positioning, spectral preprocessing method, and beam size, were investigated to improve the prediction ability of the models. The statistical results obtained for calibration models and their validation revealed that dynamic spectral acquisition and proper probe positioning were very crucial to minimize the incorporation of variability in NIR spectra resulting from the flake's undulation. Calibration and validation statistics also suggested the importance of selecting appropriate spectral preprocessing method and beam size. In this study, best calibration models resulted from standard normal variate followed by first derivative preprocessed dynamic spectra captured using beam size ~1.2 mm. Best calibration models constructed from off-line NIR spectra were used in real-time analysis of flake attributes. Finally, adequacy of best calibration models was established from real-time prediction results. Overall, with the proposed setup, it was possible to monitor the roller compaction process in real time for various properties associated with the ribbed flakes in a rapid, efficient, and nondestructive manner.

**KEY WORDS:** multivariate analysis; NIR; real-time monitoring; ribbon flakes; roller compaction.

## INTRODUCTION

Roller compaction is a popular dry granulation process for improving material flow and manufacturability without the use of heat or solvents. This granulation process is especially beneficial for moisture-sensitive and heat-sensitive active ingredients which are not suitable to be wet granulated (1,2). Roller compaction involves the use of two counter-rotating rolls which draw, compact, and consolidate the powder blend into a sheet of compacted mass or flakes. The resulting surface of the flakes can be smooth or ribbed, depending on the type of roll surfaces used. Smooth rolls are less suitable due to poorer material gripping capability. The roller compaction process has considerable advantages, including ease for continuous processing, consistent production, time scalability, and less unit operations, and therefore, has the potential to reduce manufacturing costs (3).

The fundamental mechanisms of roller compaction are complex due to the differences in the raw material properties and process variables (4–6). Raw material properties, such as particle size and morphology as well as process variables (feed screw speed, roll speed (RS), roll force (RF), roll gap, and roll surface), had been shown to affect the characteristics of the flakes which eventually affected the granules size distribution, flow characteristics, content uniformity, and compressibility after milling (3,7,8). The two main characteristics or critical quality attributes (CQA) of the flakes which are likely to affect the granule characteristics are density and strength. Impacted by all these factors, the roller-compacted product could be subjected to large variabilities. Maintenance of only constant process variables throughout the entire roller compaction operation does not necessarily guarantee the homogeneous quality flakes. In addition, the possibility of heat generation in the compaction region due to friction between the rolls and compacted powder may cause variations in the properties of the flakes during long compaction runs (9). Therefore, a deeper understanding of the process is required to reliably and consistently maintain the desired quality and product performance across a range of environments as part of a quality-by-design approach (10) and process analytical technology (PAT) initiative (11) for real-time measurements of CQA of raw and in-process materials along with process parameters. Process understanding can reduce validation burden by providing better options for justifying and qualifying systems intended to monitor and control physical and/or

[1] Department of Pharmacy, National University of Singapore, 18 Science Drive 4, Singapore 117543, Singapore.
[2] To whom correspondence should be addressed. (e-mail: phapaulh@nus.edu.sg)

chemical attributes of materials and processes. Therefore, the development and implementation of innovative technologies which enable physical and chemical analyses of roller-compacted flakes in a nondestructive, noninvasive, and real-time basis have become areas of interest by the pharmaceutical industry.

Several nondestructive monitoring techniques have been reported for monitoring the roller compaction process and they include acoustic relaxation emissions from compacted powder (12–14), thermal effusivity (9), and near-infrared (NIR) spectroscopy (15–17). Among these methods, NIR spectroscopy has gained the most interest due to its many advantages.

Quantitative NIR spectroscopic methods require the application of multivariate calibration algorithm to model spectral responses to the chemical or physical reference values of the calibration set. Spectral data and reference values are commonly designated as *X* data and *Y* data, respectively. Optimized multivariate calibration models built can then be used for the prediction or classification of unknown or new samples.

There have been considerable reports on the successful application of NIR for in-line monitoring of the roller compaction process (15,16). Gupta *et al.* reported that content uniformity, density, and tensile strength (TS) of the flakes could be predicted in-line with appropriate design of experiments and calibration model (16,18).

Most reported studies on in-line monitoring of the roller compaction process used smooth flakes rather than more industrially common ribbed flakes. Due to the sensitivity of the NIR signal to the light travel path that resulted from undulations on the flakes, the quality and variability of real-time collected NIR spectra could be affected. This may seriously affect the precision and robustness of the prediction model built based on the NIR spectra. Therefore, factors dominating the variability of the real-time collected NIR spectra in the real-time environment during calibration model development needed further investigation for the development of a robust in-line monitoring technique.

The objective of this study was to investigate the applicability of NIR spectroscopy as an in-line sensor for predicting the drug content, TS, Young's modulus ($E$), and relative density (RD) of ribbed flakes in real time. Due to the lesser sensitivity of the reflectance mode of NIR to moving sample error than transmission mode (19), the reflection mode was used in this study. The approach in this study involved three processing steps: Firstly, building the NIR partial least square (PLS1) calibration models for drug content and CQA of ribbed flakes using different off-line strategies (sampling mode: static or dynamic), spectral preprocessing methods, positioning of the probe, and beam size. Secondly, these strategies were compared in terms of their performance in calibration and validation statistics. Lastly, the best calibration models were used to predict drug content, strength, and density of ribbed flakes in real time.

## MATERIALS AND METHODS

### Materials

Chlorpheniramine maleate (BP grade, China), lactose (SpheroLac 100, Meggle, Germany), microcrystalline cellulose (MCC; Avicel PH102, FMC Biopolymer, USA), and magnesium stearate (MgSt; Sigma-Aldrich, Germany) were used in the flake formulation. Chlorpheniramine maleate was jet milled (AFG100, Hosokawa Alpine, Germany) at a pressure of 0.4 MPa and a classifying speed of 7,500 rpm to produce micronized chlorpheniramine maleate (μCPM) particles (mean diameter, ~10 μm). All experiments were performed in a controlled environment at 25±2°C and 50±5% relative humidity (RH).

### Methods

#### *Powder Blending*

A full factorial design was used to generate 25 calibration samples using a combination of formulation (μCPM concentration) and process (RF) variables at five different levels. Five different powder blends, each containing 0%, 2%, 4%, 6%, and 8%, *w*/*w* μCPM (Table I), were prepared in a 15-L intermediate bulk container (IBC) bin blender (SP15, GEA Pharma Systems, UK) with the prism attachment for 15 min at 10 rpm. MgSt was added after 10 min of blending. μCPM and lactose were premixed in a 10-L high shear mixer (UltimaPro 10, Collette NV, Belgium) at an impeller speed of 200 rpm for 3 min prior to mixing with MCC and MgSt in the IBC. Addition of MgSt to the powder blend before roller compaction is a common practice in pharmaceutical industry to prevent sticking of compacted powders to the roll surfaces, especially when the roll surfaces are not smooth (20–23).

#### *Roller Compaction of Powder Blends*

Each powder blend prepared was compacted at five different (40, 50, 60 70, and 80 kN) RFs on a roller compactor (Pharmapaktor L200/30P, Hosokawa Bepex, Germany) fitted with rolls of 20 cm diameter and 3 cm width axially corrugated roll surfaces. The roller compactor was operated in the automatic mode using an RS of 2.6 rpm. With the automatic mode, the speed of the vertical feeding screw was automatically controlled by a feedback system to maintain the desired RF at an RS of 2.6 rpm. For each run, the roller compactor was allowed to reach steady state, about 1 min, before actual sample collection and RF recording at every second in the subsequent 5 min and averaged for the reference value. For the study, the flakes produced were subjected to vibration for the removal of uncompacted material on a 2-mm aperture-sized mesh of a sieve shaker (KS 1000, Retsch, Germany) set at 70 shakes/min for 2 min. The sieved flakes were then stored

**Table I.** Composition of Formulations

| | Component (%, *w*/*w*) | | | |
|---|---|---|---|---|
| Formulation | μCPM | Lactose | MCC | MgSt |
| 1 | 0 | 49 | 50 | 1 |
| 2 | 2 | 47 | 50 | 1 |
| 3 | 4 | 45 | 50 | 1 |
| 4 | 6 | 43 | 50 | 1 |
| 5 | 8 | 41 | 50 | 1 |

at 25±2°C and 50±5% RH until required for analysis for at least 3 days.

*Flake Density Measurements*

True densities ($\rho^T$) of the powder components (μCPM, lactose, MCC, and MgSt) were determined using a helium pycnometer (Pentapycnometer, Quantochrome Instuments, USA). True densities of μCPM powder blends ($\rho^T_{blend}$) were calculated by taking the weighted mean of the true densities of μCPM ($\rho^T_{\mu CPM}$), lactose ($\rho^T_{lactose}$), MCC ($\rho^T_{MCC}$), and MgSt ($\rho^T_{MgSt}$) using Eq. 1:

$$\rho^T_{blend} = c_1\rho^T_{\mu CPM} + c_2\rho^T_{lactose} + c_3\rho^T_{MCC} + c_4\rho^T_{MgSt} \quad (1)$$

where $c_1$, $c_2$, $c_3$, and $c_4$ are the weight fractions of μCPM, lactose, MCC, and MgSt in the powder blends, respectively. The method of calculation was also used by Gupta *et al.* to calculate the true densities of powder blends (16).

Several methods are available to measure the degree of material densification of compacted ribbons. One widely used method is the displacement method. There is a commercially available equipment, the GeoPyc 1360 pycnometer, invented by Micromeritics which uses the plunger system to compact the material bed horizontally at a predetermined force. The difference between the distance advanced by the plunger with and without the particle will be transmitted into a signal to calculate the envelope volume of the particle. The GeoPyc® 1360 pycnometer has been used by several researchers for the determination of envelope density of ribbed roller compacted flakes (21,24).

In our laboratory, flake envelop density (ED) based on the previous displacement method was obtained using a universal powder tester (FT4 Powder Rheometer, Freeman Technology, UK). This tester allowed accurate envelope volume measurements of irregular objects by a method analogous to volume measurement by fluid displacement. This was facilitated through an assembly consisting of a cylindrical sample chamber (50 mm diameter), a plunger, and glass beads (JM 13, Pan Abrasives, Singapore) as displacement medium. Seven pieces of flakes were used for the flake density measurement in each run. The length and width of each flake were 43 and 30 mm, respectively. At first, the flakes were placed vertically inside the cylindrical sample chamber followed by filling of the remaining portion of the chamber by glass beads. Since the batch of glass beads of particle size, 32.6±0.5 μm, was free flowing, it filled all the voids, allowing the determination of solid or envelope volume of large irregular objects. A normal stress of 21.7 kPa was selected for all the measurements. Modest consolidation pressures were applied during measurements to facilitate medium conformation to the sample surface without inducing sample dimensional changes. ED of a flake in a sample was calculated from the envelope volume and weight of the flakes. Flakes and glass beads were dried overnight in a hot-air oven at 60°C and left to equilibrate to ambient temperature in a desiccator at least overnight prior to analysis. Flake RDs were calculated by using Eq. 2:

$$RD = \frac{ED}{\rho^T_{blend}} \quad (2)$$

Three determinations were obtained and the results were averaged for the reference value for each batch of flakes.

*Flake Strength Measurements*

Flake strength measurements were carried out using the three-point beam bending method on the universal testing machine (EZ Test 100 N, Shimadzu, Japan) with a 100-N load cell. The gap length ($L$) between the lower two supports was kept constant at 25 mm. Data were collected using the WinAGS Lite (version 1.00) software supplied with the instrument. The acquisition rate was 200 points/s at a test speed of 1 mm/s. Maximum load ($P$) required for fracturing the flake, as well as the deflection ($y$) of the load point at the fracture were obtained from the universal testing machine readings. Width ($b$) and thickness ($h$) were measured for all flakes prior to flexure testing. TS and Young's modulus ($E$) were calculated from the above values using Eqs. 3 and 4, respectively.

$$TS = \frac{3PL}{2bh^2} \quad (3)$$

$$E = \frac{PL^3}{4bh^3y} \quad (4)$$

Fifteen measurements were obtained for each batch of flakes and the results were averaged for the reference values.

*Flake Thickness Measurement*

Peak to peak thickness of 10 flakes stack was measured by using a digital caliper (Digimatic, Mitutoyo, Japan). Flakes of approximately 30×30 mm squares were stacked with ridges of alternate flakes perpendicularly aligned. Measurements were repeated for 10 different stacks for each batch of flakes and the results were averaged.

*NIR Spectroscopy*

The optical sensing system, which was used to obtain the diffuse NIR reflection spectra from the flakes, consisted of an NIR diffuse reflectance measurement probe coupled with an NIR spectral sensor (MCS 611 NIR 2.2, Carl Zeiss, Germany) and a tungsten halogen light source (LS-1-LL, Ocean Optics, USA). The NIR diffuse reflectance measurement probe consisted of a tight bundle of six illumination fibers (each around one read fiber) in a stainless steel ferrule. Three NIR diffuse reflectance measurement probes, QR 200, QR 400, and QR 600 (QR 200-7-VIS-BX; QR 400-7-VIS-BX; QR 600-7-VIS125BX, Ocean Optics, USA), differing in their fiber core diameters of 200±4, 400±8, and 600±10 μm, respectively, were used for this study. The fiber bundle external diameters or the beam sizes of QR 200, QR 400, and QR 600 were ~0.6, 1.2, and 1.8 mm, respectively. The setup used allowed the spectral acquisition of 980–1,900 nm with 1 nm resolution at an integration time or spectra acquisition time of 100 ms.

*Off-line NIR Monitoring Setup*

A custom-made conveyor belt was fabricated for off-line spectral acquisition from flakes (Fig. 1). The conveyor system consisted of a pair of parallel conveying belts rotated by two 3-cm-thick roller. A 1-cm gap between these two parallel conveying belts was always maintained to allow NIR spectra acquisition from the underside (base) of the sample. A support platform was placed under the belts to minimize vertical movements of the belts. The fiber optic probe was mounted just before the terminal end of the conveying belt. Strips of the compacted flakes were lined along the conveying belts for NIR spectral acquisition. A clearance of 1 mm (QR 200 and QR 400) or 0.5 mm (QR 600) between the flake and probe was always maintained to avoid errors associated with the sampling distance. The NIR spectra were collected from the upper side of the flakes (Fig. 1a), as well as from the underside of the flakes (Fig. 1b). Two types of sampling mode, static and dynamic, were used to collect the NIR spectra from flakes. The static NIR spectra were captured from the different segments of the flake when the flake was placed on the stationery conveyor belt. The dynamic NIR spectra were captured when the flakes were moving with the conveyor system at a constant velocity, equivalent to the RS of 2.6 rpm to simulate the conditions during NIR real-time monitoring of the roller compaction process. Diffuse reflection spectra were acquired through the fiber optic probe and processed on a computer using the Aspect Plus (version 1.76, Carl Zeiss, Germany) and Process Explorer (version 1.1.0.6, Carl Zeiss, Germany) softwares. In the Process Explorer method setup, a trend qualification rule was set to remove the nonrepresentative spectra from the data stream. Sometimes, nonrepresentative spectra resulted during spectra acquisition due to triggering of the NIR sensor in between the ends of two consecutive flakes moving along the conveying belts. From each calibration batch, 30 representative NIR spectra were captured in each sampling mode, probe position, and probe diameter for calibration model development and validation.

*Calibration Model Development from the Off-line NIR Spectral Data*

Unscrambler (version 9.8, Camo Software AS, Norway) was used off-line to build the calibration models. The raw calibration spectra were preprocessed using standard normal variate (SNV) followed by derivative preprocessing. All first and second derivative spectra were computed employing seven smoothening points and second polynomial order. PLS1 regression technique was used to build the calibration models for the μCPM concentration, TS, *E*, and RD of the flakes. A global model was built for μCPM concentration from whole data set, whereas for other flake attributes, one model was built for each μCPM concentration (0%, 2%, 4%, 6%, and 8%, *w*/*w*). Formulations 1 to 5 (Table I) could behave very differently under compression due to the variation in the ratio of lactose and MCC. This variation could affect the CQA of

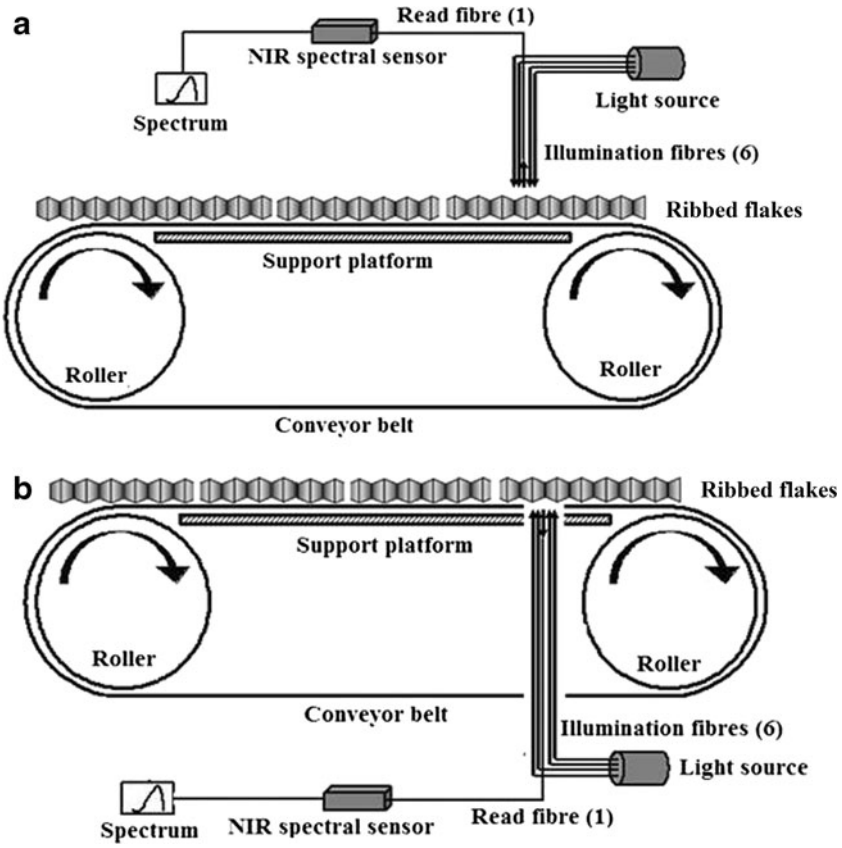


**Fig. 1.** Schematic diagram of NIR off-line setup for spectral acquisition from the upper side of the flakes (**a**) and the underside of the flakes (**b**). During spectra acquisition from the underside of the flakes (**b**), NIR probe was placed in between two parallel conveying belts from the bottom of the conveyor system

flakes but not the μCPM concentration. Due to this reason, a global calibration model for μCPM concentration including all 25 batches was constructed, whereas for CQA, one model was built for each μCPM concentration (0%, 2%, 4%, 6%, and 8%, *w*/*w*) to avoid confounding. One model for each subgroup was reported to be more accurate when the data set consists of several separate subgroupings (25).

*Validation of the Calibration Models*

The test set validation (TSV) method was used to validate the calibration models of μCPM concentration and CQA of flakes. By this method, the global data set was split into two subsets, calibration and test sets. Thirty NIR spectra were captured from each batch of flakes using different sampling strategies, positioning of NIR probes, and beam size during off-line spectra acquisition. The first 20 NIR spectra of a batch were taken for calibration and the remaining 10 NIR spectra were taken for TSV. The calibration set was used to build the calibration model using *X* (spectra) and *Y* (reference) values. Next, *X* values of the test set were fed into the model to compute new components. Their predicted *Y* values were then compared to the observed *Y* values, yielding prediction residuals which were used to compute a validation residual variance or a root mean square error of prediction (RMSEP).

*μCPM Content Uniformity Determination of Flakes*

Five pieces of scanned flakes from each calibration batch were randomly selected for the μCPM content uniformity determination. A laboratory-validated ultraviolet (UV) spectroscopic method was used to calculate the μCPM content uniformity of each batch of flakes. A midportion of approximately 1×1 cm was cut from each flake and crushed into powder. An accurately weighed powder sample of 500 mg was transferred in volumetric flask and 200 ml distilled water was added. The flask was then shaken and ultrasonicated for 10 min till complete disintegration and dissolution of the active ingredients. Approximately 20 ml aliquot was withdrawn and centrifuged at 2,000 rpm for 5 min, and the resulting supernatant solution was analyzed for CPM content by UV absorption (UV-3101 PC, Shimadzu, Japan) at 262 nm. Twenty-five measurements were obtained for each μCPM concentration and the results were averaged for reference values.

*Real-Time NIR monitoring Setup*

A rectangular channel (Fig. 2) was used to guide the flake released after roller compaction. The flowing motion of the flake was well guided by pushing to one inner side wall of the channel using brushes fitted inside the channel. NIR spectra were captured from the side of the moving flake, which always touched the inner side wall. The side of the moving flake touching the inner side wall was chosen for spectral acquisition to maintain a constant gap between the flake surface and probe head. The probe was kept perpendicular and on the middle point of the face of the flakes such that the sensor received the reflected beams without any stray effects. A gap of 1 mm (QR 200 and QR 400) or 0.5 mm (QR 600) was always maintained between the channel inner surface on which the flakes were moving and the probe head. In addition, the channel was fitted with a plastic cover and a light vacuum suction was maintained on the top to remove surface powder and prevent powder cloud formation in spectral acquisition zone.

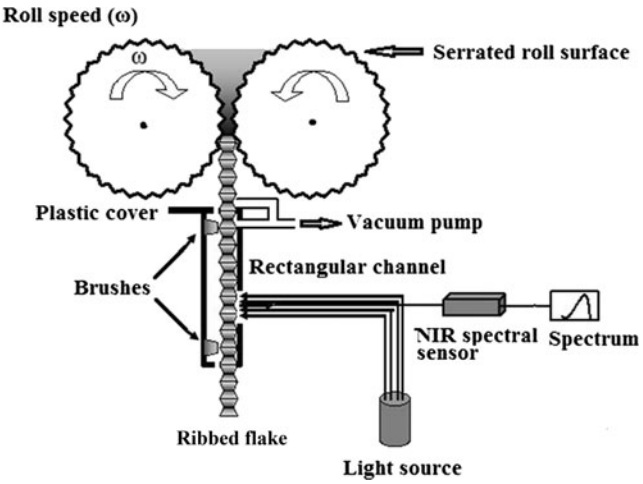


**Fig. 2.** Schematic diagram of in-line NIR monitoring setup for real-time roller compaction process

*Real-Time Monitoring Using Online Unscrambler Predictor (OLUP) Software*

Real-time analysis was carried out to assess the developed NIR models for their capability to quantitatively predict the flake properties using the setup illustrated in Fig. 2. Prior to experimentation, the final calibration models were uploaded into the Process Explorer using the OLUP software. The OLUP packaged the Unscrambler calibration models as a dynamic link library (32 bit only) protocol. Through these protocols, Process Explorer was interfaced with the OLUP for producing real-time prediction of flake properties. During real-time measurements, raw energy spectra were obtained from the light signals through the fiber optic probe using the MCS 611 NIR 2.2 spectral sensor (Carl Zeiss, Germany) and transferred the acquired spectra using radio frequency to the nearby microprocessor using the Aspect Plus (version 1.76, Carl Zeiss, Germany) and Process Explorer (version 1.1.0.6, Carl Zeiss, Germany) softwares.

For real-time analysis of μCPM concentration in compacted flakes, batches of 500 g powder blends containing 0%, 2%, 4%, 6%, or 8%, *w*/*w* μCPM were roller compacted sequentially with increasing concentration of μCPM. RS and RF were set to 2.6 rpm and 60 kN, respectively. During roller compaction, the powder blends were poured into the hopper just before finishing compaction of the previous blend in order to limit the mixing of two consecutive blends. A cylindrical tube (30 mm diameter) was present between the hopper and the main compaction zone. Inside this cylindrical tube, the force feeding screw (27.5 mm diameter) rotated to convey the powder from the hopper to the main compaction zone. During real-time analysis, a powder blend of higher μCPM concentration was added when the level of the previous blend was inside this cylindrical region. Inside this cylindrical region,

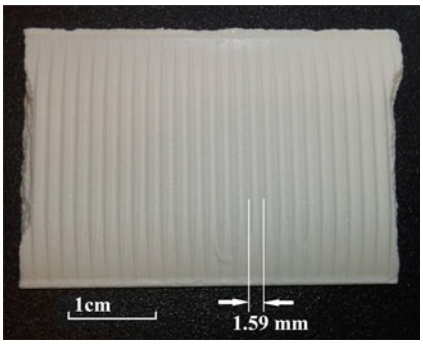


**Fig. 3.** Top view of ribbed roller-compacted flake

the chances of transitional mixing of two consecutive blends were less due to the precompaction of the powder in this narrow region.

For real-time analysis of TS, *E*, and RD of compacted flakes, the powder blend containing 4%, *w*/*w* μCPM was roller compacted for 2 min at each RF (40, 50, 60, 70, and 80 kN) in a chronologically increasing order. NIR spectra were captured every 5 s during real-time analyses. Therefore, real-time analysis of μCPM and CQA of flakes was done for ~16 and 10 min, respectively. In total, real-time analysis was for ~26 min.

## RESULTS AND DISCUSSION

### Linear Effective Surface Area Scanned by Different NIR Probes

The linear effective surface area was calculated instead of actual effective surface area measurement due to the undulations on the flake surface. The actual effective surface area is the total area of the flake surface based on curved faces. On the other hand, linear effective surface area was determined by simply considering the length and width of the flake surface in a linear scale. Figure 3 depicts the surface texture of the ribbed flake produced by axially corrugated rolls. The ribbed flake surface consisted of evenly distributed peaks and troughs. The distance between two consecutive peaks or troughs was 1.59 mm (Fig. 3). In a static sampling mode, the shape of the scanned area is circle and, therefore, linear effective surface areas of flakes scanned by QR 200, QR 400, and QR 600 probes were calculated using Eq. 5 and the values

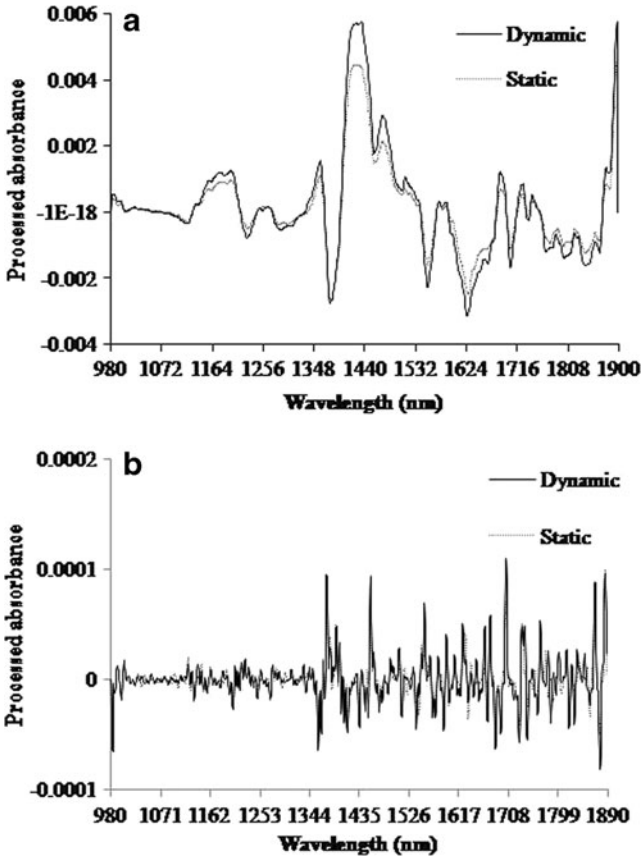


**Fig. 5.** Spectral difference observed for the same piece of flake with dynamic and static sampling strategies. Spectra were captured from the upper side of the flakes using QR 400 probe. **a** SNV followed by first derivative spectra and **b** SNV followed by second derivative spectra

of the scanned areas were 0.28, 1.13, and 2.55 $mm^2$, respectively. In dynamic sampling mode, the shape of the scanned area was like Fig. 4 and linear effective surface areas scanned by the three NIR probes were determined based on the distances traveled by the moving flakes under the illuminated spots of 0.6 mm (QR 200), 1.2 mm (QR 400), and 1.8 mm (QR 600) diameters of the NIR probes in 100 ms integration time periods. In this study, 100 ms integration time was chosen for both off-line and real-time spectral acquisition. In this specified integration time interval, the distance traveled

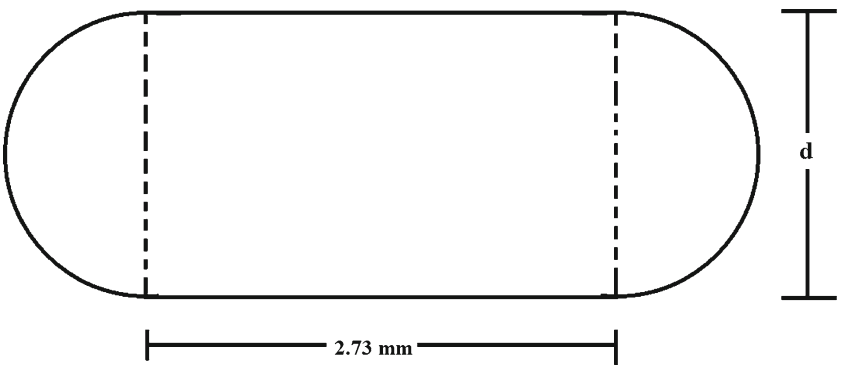


**Fig. 4.** Schematic diagram of shape of scanned area by NIR probe (*d* diameter of probe) in dynamic mode

by the moving flakes under the illuminated spots of NIR probes was 2.73 mm calculated from the roller speed (2.6 rpm) and roller diameter (20 cm). Considering the experimental conditions used, it was estimated that, during a scan run of the flake surface, all the spots of the probes would traverse a distance of 2.73 mm which was greater than two consecutive peaks or trough distances across the flake surface. Thus, the linear effective surface areas, i.e., area sampled by QR 200, QR 400, and QR 600 NIR probes, were 1.92, 4.41, and 7.46 $mm^2$, respectively, calculated using Eq. 6. The first term $\left(\frac{\pi d^2}{4}\right)$ in the Eq. 6 represents the total area of two half circles situated on the two sides of the midrectangular portion and the second term $(2.73d)$ represents the area of the rectangular portion of the scanned area (Fig. 4).

$$\text{Linear effective surface area(Static sampling mode)} = \frac{\pi \mathrm{d}^2}{4} \quad (5)$$

$$\text{Linear effective surface area(Dynamic sampling mode)} = \frac{\pi \mathrm{d}^2}{4} + 2.73\mathrm{d} \quad (6)$$

where $d$ is the beam size or illuminated spot diameter of the NIR probe in millimeters.

Therefore, it was advantageous to use the dynamic sampling mode as it enabled the scanning of a larger flake surface area than the equivalent stationery illuminated spot measurement. In addition, the dynamic sampling mode might be a helpful approach to improve the performances of the calibration models by minimizing the errors associated with the undulations on the flake surface. Furthermore, from the use of probes with different dimensions, it was possible to determine the occurrence of nonuniform drug distribution resulting from the agglomeration of very fine μCPM particles (about 10 μm) which would not have been feasible with analysis of the whole area of the flake surface. In an investigation, Li *et al.* demonstrated that spectral analysis of small portions of the tablet is an acceptable replacement for whole-tablet analysis using traditional high-performance liquid chromatography/UV quantitative content determination (26).

### Effect of Sampling Mode on NIR Spectral Feature and Calibration Models

Experiments were carried out to examine the effect of sampling modes (static and dynamic) on the NIR spectral features of the flakes. The flakes from all the calibration batches were subjected to NIR spectral acquisition using static and dynamic modes from both the upper side and the under-

**Table II.** Summary of the Figures of Merit Obtained for Calibration Models Based on SNV Followed by First Derivative Pretreated Spectra in Static Mode

| | | Calibration | | | Validation | | |
|---|---|---|---|---|---|---|---|
| Parameter | No. of PC | $R^2$ | $X$ (%) | RMSEC | $R^2$ | $X$ (%) | RMSEP |
| QR 200 (upper side) | | | | | | | |
| μCPM | 3 | 0.844 | 57.37 | 1.109 | 0.818 | 58.02 | 1.194 |
| TS (4% μCPM) | 3 | 0.870 | 66.85 | 0.103 | 0.626 | 61.00 | 0.186 |
| $E$ (4% μCPM) | 3 | 0.860 | 66.94 | 1.394 | 0.627 | 60.97 | 2.422 |
| RD (4% μCPM) | 3 | 0.780 | 67.93 | 0.014 | 0.447 | 62.28 | 0.022 |
| QR 200 (underside) | | | | | | | |
| μCPM | 10 | 0.945 | 84.44 | 0.655 | 0.713 | 79.39 | 1.500 |
| TS (4% μCPM) | 9 | 0.994 | 86.34 | 0.024 | 0.613 | 78.48 | 0.189 |
| $E$ (4% μCPM) | 7 | 0.994 | 86.33 | 0.296 | 0.613 | 78.49 | 2.461 |
| RD (4% μCPM) | 5 | 0.887 | 81.53 | 0.010 | 0.641 | 75.84 | 0.018 |
| QR 400 (upper side) | | | | | | | |
| μCPM | 4 | 0.861 | 83.54 | 1.042 | 0.929 | 82.34 | 0.746 |
| TS (4% μCPM) | 3 | 0.658 | 84.10 | 0.178 | 0.548 | 76.43 | 0.204 |
| $E$ (4% μCPM) | 3 | 0.643 | 84.14 | 2.362 | 0.549 | 76.29 | 2.655 |
| RD (4% μCPM) | 4 | 0.861 | 89.82 | 0.011 | 0.586 | 80.02 | 0.019 |
| QR 400 (underside) | | | | | | | |
| μCPM | 4 | 0.932 | 82.00 | 0.732 | 0.906 | 73.90 | 0.860 |
| TS (4% μCPM) | 8 | 0.896 | 97.30 | 0.098 | 0.714 | 91.79 | 0.163 |
| $E$ (4% μCPM) | 8 | 0.894 | 97.30 | 1.285 | 0.703 | 91.79 | 2.155 |
| RD (4% μCPM) | 7 | 0.926 | 96.50 | 0.008 | 0.873 | 91.05 | 0.011 |
| QR 600 (upper side) | | | | | | | |
| μCPM | 4 | 0.957 | 81.20 | 0.580 | 0.945 | 70.63 | 0.655 |
| TS (4% μCPM) | 2 | 0.516 | 73.89 | 0.212 | 0.324 | 52.24 | 0.250 |
| $E$ (4% μCPM) | 2 | 0.510 | 73.88 | 2.767 | 0.319 | 52.39 | 3.262 |
| RD (4% μCPM) | 4 | 0.768 | 81.05 | 0.014 | 0.401 | 41.89 | 0.023 |
| QR 600 (underside) | | | | | | | |
| μCPM | 4 | 0.873 | 86.69 | 1.000 | 0.903 | 85.06 | 0.870 |
| TS (4% μCPM) | 4 | 0.666 | 91.72 | 0.176 | 0.534 | 81.82 | 0.208 |
| $E$ (4% μCPM) | 4 | 0.671 | 91.69 | 2.268 | 0.526 | 81.85 | 2.721 |
| RD (4% μCPM) | 3 | 0.732 | 86.98 | 0.015 | 0.638 | 71.18 | 0.018 |

side of the flakes, perpendicular to the flake surface. The obtained spectra were pretreated with SNV followed by first derivative and SNV followed by second derivative preprocessing. Careful examination of the spectra (Fig. 5) obtained using different strategies showed the exhibition of certain spectral differences. The observed spectral differences illustrated the importance of adopting appropriate and similar sampling strategies for both calibration and actual testing for use in the real-time roller compaction process.

All the models built using different strategies were compared to determine the appropriate sampling mode and preprocessing method for finding the optimal calibration models. Performances of the models were compared on the basis of figures of merits as shown in Tables II, III, IV, and V. A superior calibration model always exhibit lower root mean square error of calibration (RMSEC) and RMSEP values employing less number of principal components (PC). In these tables, the calibration models of TS, *E*, and RD built from 4%, *w*/*w* μCPM-containing flakes were only compared. Maximum variabilities in CQA were observed with the flakes produced from 4%, *w*/*w* μCPM powder blend among the five different concentrations of μCPM studied. Maximum variabilities were reflected with the higher values of RMSEC and RMSEP values of off-line calibration models. In order to introduce maximum variability and make a more representative model for the prediction of CQA, the batch with 4%, *w*/*w* μCPM was chosen. The calibration models built from static sampling mode showed inferior performance in terms of figures of merits, especially the validation results, irrespective of the spectral preprocessing technique for all types of NIR probes. This is quite interesting as most of the previous studies based on static spectral acquisition reported improved performances of the models due to their smooth surface of the flakes (16,18,22,27,28). In this study, the performances of the models were poorer when the models were built using static spectral data. This could also be due to the differences in NIR light travel path lengths during each static spectral acquisition from the ribbed flake surface. In dynamic spectral acquisition, performances of models were improved as the differences in NIR light travel path lengths were compensated by the continuous movement of the flake surfaces during measurements. Hence, it was more appropriate to capture the NIR spectra of the calibration batches in a dynamic mode, which also simulated the movement of flakes as in the real-time roller compaction process.

### Effect of Preprocessing Method on Calibration Models

In NIR spectroscopy, the choices of spectral regions and spectral preprocessing methods to be used for building the calibration models are of great importance. In this study, the entire wavelength range (980–1,900 nm) was used to build the

**Table III.** Summary of the Figures of Merit Obtained for Calibration Models Based on SNV Followed by First Derivative Pretreated Spectra in Dynamic Mode

| | | Calibration | | | Validation | | |
|---|---|---|---|---|---|---|---|
| Parameter | No. of PC | $R^2$ | *X* (%) | RMSEC | $R^2$ | *X* (%) | RMSEP |
| QR 200 (upper side) | | | | | | | |
| μCPM | 4 | 0.948 | 78.63 | 0.638 | 0.944 | 78.10 | 0.663 |
| TS (4% μCPM) | 4 | 0.981 | 78.91 | 0.042 | 0.929 | 75.54 | 0.070 |
| *E* (4% μCPM) | 4 | 0.978 | 79.10 | 0.589 | 0.918 | 75.79 | 0.975 |
| RD (4% μCPM) | 4 | 0.980 | 80.06 | 0.004 | 0.955 | 70.06 | 0.006 |
| QR 200 (underside) | | | | | | | |
| μCPM | 3 | 0.958 | 65.69 | 0.577 | 0.956 | 64.27 | 0.585 |
| TS (4% μCPM) | 5 | 0.981 | 82.87 | 0.041 | 0.927 | 75.67 | 0.074 |
| *E* (4% μCPM) | 5 | 0.980 | 82.97 | 0.564 | 0.938 | 97.97 | 0.902 |
| RD (4% μCPM) | 4 | 0.976 | 81.70 | 0.005 | 0.963 | 97.59 | 0.006 |
| QR 400 (upper side) | | | | | | | |
| μCPM | 2 | 0.962 | 83.48 | 0.549 | 0.968 | 82.92 | 0.502 |
| TS (4% μCPM) | 4 | 0.957 | 97.08 | 0.064 | 0.901 | 95.90 | 0.091 |
| *E* (4% μCPM) | 4 | 0.946 | 97.13 | 0.931 | 0.909 | 95.88 | 1.134 |
| RD (4% μCPM) | 3 | 0.955 | 94.91 | 0.006 | 0.963 | 94.42 | 0.006 |
| QR 400 (underside) | | | | | | | |
| μCPM | 2 | 0.993 | 70.17 | 0.230 | 0.994 | 68.73 | 0.224 |
| TS (4% μCPM) | 4 | 0.959 | 95.99 | 0.058 | 0.949 | 94.50 | 0.069 |
| *E* (4% μCPM) | 4 | 0.971 | 95.84 | 0.647 | 0.939 | 93.72 | 0.904 |
| RD (4% μCPM) | 4 | 0.976 | 94.31 | 0.005 | 0.966 | 92.27 | 0.006 |
| QR 600 (upper side) | | | | | | | |
| μCPM | 3 | 0.954 | 82.95 | 0.596 | 0.956 | 77.75 | 0.586 |
| TS (4% μCPM) | 7 | 0.965 | 96.51 | 0.058 | 0.885 | 90.42 | 0.103 |
| *E* (4% μCPM) | 7 | 0.963 | 96.29 | 0.774 | 0.888 | 88.78 | 1.325 |
| RD (4% μCPM) | 5 | 0.979 | 95.31 | 0.004 | 0.950 | 86.74 | 0.007 |
| QR 600 (underside) | | | | | | | |
| μCPM | 3 | 0.963 | 85.46 | 0.536 | 0.958 | 78.17 | 0.576 |
| TS (4% μCPM) | 5 | 0.928 | 95.52 | 0.082 | 0.888 | 88.96 | 0.083 |
| *E* (4% μCPM) | 5 | 0.931 | 95.57 | 1.039 | 0.928 | 89.03 | 1.060 |
| RD (4% μCPM) | 4 | 0.916 | 90.97 | 0.009 | 0.929 | 78.73 | 0.008 |

**Table IV.** Summary of the Figures of Merit Obtained for Calibration Models Based on SNV Followed by Second Derivative Pretreated Spectra in Static Mode

| | | Calibration | | | Validation | | |
|---|---|---|---|---|---|---|---|
| Parameter | No. of PC | $R^2$ | $X$ (%) | RMSEC | $R^2$ | $X$ (%) | RMSEP |
| QR 200 (upper side) | | | | | | | |
| μCPM | 3 | 0.861 | 22.97 | 1.043 | 0.788 | 19.61 | 1.289 |
| TS (4% μCPM) | 3 | 0.913 | 31.27 | 0.087 | 0.475 | 20.82 | 0.220 |
| *E* (4% μCPM) | 3 | 0.912 | 31.38 | 1.144 | 0.473 | 20.85 | 2.870 |
| RD (4% μCPM) | 3 | 0.881 | 30.79 | 0.010 | 0.368 | 19.42 | 0.024 |
| QR 200 (underside) | | | | | | | |
| μCPM | 4 | 0.859 | 44.80 | 1.054 | 0.716 | 35.74 | 1.492 |
| TS (4% μCPM) | 5 | 0.968 | 55.35 | 0.055 | 0.660 | 32.63 | 0.177 |
| *E* (4% μCPM) | 5 | 0.970 | 55.35 | 0.686 | 0.665 | 32.79 | 2.286 |
| RD (4% μCPM) | 4 | 0.894 | 54.98 | 0.010 | 0.676 | 29.03 | 0.017 |
| QR 400 (upper side) | | | | | | | |
| μCPM | 4 | 0.895 | 80.80 | 0.907 | 0.939 | 79.24 | 0.689 |
| TS (4% μCPM) | 3 | 0.695 | 79.74 | 0.168 | 0.183 | 54.25 | 0.275 |
| *E* (4% μCPM) | 3 | 0.693 | 79.49 | 2.189 | 0.205 | 54.26 | 3.523 |
| RD (4% μCPM) | 3 | 0.856 | 79.40 | 0.011 | 0.363 | 54.00 | 0.024 |
| QR 400 (underside) | | | | | | | |
| μCPM | 4 | 0.873 | 72.57 | 0.999 | 0.901 | 58.86 | 0.883 |
| TS (4% μCPM) | 6 | 0.908 | 86.66 | 0.092 | 0.574 | 67.66 | 0.198 |
| *E* (4% μCPM) | 6 | 0.907 | 86.62 | 1.203 | 0.570 | 67.68 | 2.593 |
| RD (4% μCPM) | 5 | 0.924 | 84.62 | 0.008 | 0.819 | 66.02 | 0.013 |
| QR 600 (upper side) | | | | | | | |
| μCPM | 6 | 0.963 | 79.66 | 0.542 | 0.944 | 71.81 | 0.663 |
| TS (4% μCPM) | 3 | 0.573 | 69.83 | 0.199 | 0.410 | 52.86 | 0.234 |
| *E* (4% μCPM) | 3 | 0.569 | 69.67 | 2.594 | 0.404 | 52.65 | 3.052 |
| RD (4% μCPM) | 3 | 0.629 | 70.21 | 0.018 | 0.551 | 53.81 | 0.020 |
| QR 600 (underside) | | | | | | | |
| μCPM | 5 | 0.906 | 77.12 | 0.858 | 0.923 | 76.18 | 0.778 |
| TS (4% μCPM) | 6 | 0.896 | 87.41 | 0.098 | 0.570 | 71.10 | 0.199 |
| *E* (4% μCPM) | 6 | 0.906 | 87.41 | 1.209 | 0.567 | 71.15 | 2.602 |
| RD (4% μCPM) | 6 | 0.884 | 88.45 | 0.010 | 0.521 | 63.79 | 0.021 |

calibration models. It is a general principle that a parsimonious model, a model with fewer components and variables than the full components or variables, will result in a model with optimal calibration statistics since the number of model parameter is sparse. However, it could be advantageous in some cases to keep some of the wavelengths with even the slightest correlation with respect to the component to span the multidimensional space, especially when the sample is moving or varies rapidly with time (25,29,30). Figure 6 shows that all the flake components exhibited regions of meaningful correlations throughout the entire wavelength range, but almost all the regions are overlapping. On the other hand, spectral preprocessing is usually performed to remove unwanted scattering features incorporated in NIR spectra which are often due to the differences in sizes of the constituent particles and other interfering factors (31–33). Two commonly used preprocessing methods for diffuse reflectance spectra are SNV and multiple scatter correction (MSC). Since the MSC normalizes based on the mean spectrum in a data set, it is best suited for similar sample sets. Therefore, SNV was selected as the preferred preprocessing method for NIR spectra in this study. Derivative preprocessing was applied after SNV treatment to correct the baseline effects in spectra for the purpose of removing nonchemical effects and creating robust calibration models. In addition, derivatives may also aid in resolving overlapped bands. Figure 7a–d shows the raw, SNV, SNV followed by first derivative, and SNV followed by second derivative preprocessed spectra of calibration batches of flakes for the entire spectral range of 980–1,900 nm, respectively. Figure 7c, d depicts the corrections of both shift and curvature of the baselines obtained after processing the spectra with SNV followed by derivative preprocessing.

In the case of NIR-PLS1 calibration models built from dynamic NIR spectra of three different probes, the performances of calibration models were found to be better when SNV followed by first derivative was used (Table III). The RMSEC and RMSEP values were found to be decreased considerably with these calibration models employing less number of PC. In addition, low $X$ explained variances were observed with the calibration models built using SNV followed by second derivative spectra (Table V).

### Effect of Probe Position on Calibration Models

The NIR-PLS1 calibration models built from the dynamic spectra collected from the upper side and the underside of the

**Table V.** Summary of the Figures of Merit Obtained for Calibration Models Based on SNV Followed by Second Derivative Pretreated Spectra in Dynamic Mode

| | | Calibration | | | Validation | | |
|---|---|---|---|---|---|---|---|
| Parameter | No. of PC | $R^2$ | $X$ (%) | RMSEC | $R^2$ | $X$ (%) | RMSEP |
| QR 200 (upper side) | | | | | | | |
| μCPM | 4 | 0.933 | 37.23 | 0.725 | 0.919 | 33.88 | 0.796 |
| TS (4% μCPM) | 3 | 0.937 | 36.00 | 0.077 | 0.856 | 14.46 | 0.107 |
| *E* (4% μCPM) | 3 | 0.933 | 37.50 | 1.021 | 0.774 | 15.49 | 1.880 |
| RD (4% μCPM) | 4 | 0.986 | 39.69 | 0.004 | 0.901 | 17.65 | 0.009 |
| QR 200 (underside) | | | | | | | |
| μCPM | 3 | 0.956 | 29.67 | 0.585 | 0.930 | 25.96 | 0.740 |
| TS (4% μCPM) | 4 | 0.964 | 38.79 | 0.058 | 0.892 | 21.08 | 0.093 |
| *E* (4% μCPM) | 3 | 0.936 | 32.54 | 1.001 | 0.881 | 19.15 | 1.268 |
| RD (4% μCPM) | 5 | 0.974 | 38.40 | 0.005 | 0.932 | 21.96 | 0.008 |
| QR 400 (upper side) | | | | | | | |
| μCPM | 2 | 0.968 | 71.25 | 0.498 | 0.973 | 68.97 | 0.463 |
| TS (4% μCPM) | 5 | 0.976 | 81.85 | 0.047 | 0.821 | 77.72 | 0.129 |
| *E* (4% μCPM) | 5 | 0.982 | 82.32 | 0.531 | 0.847 | 77.52 | 1.545 |
| RD (4% μCPM) | 2 | 0.947 | 76.10 | 0.007 | 0.963 | 75.94 | 0.006 |
| QR 400 (underside) | | | | | | | |
| μCPM | 2 | 0.981 | 33.65 | 0.384 | 0.975 | 30.44 | 0.443 |
| TS (4% μCPM) | 4 | 0.978 | 74.64 | 0.044 | 0.811 | 64.75 | 0.121 |
| *E* (4% μCPM) | 4 | 0.978 | 97.79 | 0.571 | 0.799 | 79.90 | 1.773 |
| RD (4% μCPM) | 3 | 0.983 | 57.00 | 0.004 | 0.939 | 51.14 | 0.007 |
| QR 600 (upper side) | | | | | | | |
| μCPM | 3 | 0.950 | 62.54 | 0.627 | 0.954 | 57.68 | 0.604 |
| TS (4% μCPM) | 2 | 0.512 | 69.56 | 0.212 | 0.558 | 53.96 | 0.202 |
| *E* (4% μCPM) | 2 | 0.498 | 69.43 | 2.802 | 0.539 | 53.81 | 2.684 |
| RD (4% μCPM) | 5 | 0.987 | 75.73 | 0.003 | 0.853 | 58.57 | 0.011 |
| QR 600 (underside) | | | | | | | |
| μCPM | 3 | 0.958 | 71.06 | 0.572 | 0.967 | 64.85 | 0.508 |
| TS (4% μCPM) | 6 | 0.985 | 89.82 | 0.037 | 0.953 | 74.87 | 0.066 |
| *E* (4% μCPM) | 6 | 0.985 | 89.88 | 0.488 | 0.952 | 75.13 | 0.863 |
| RD (4% μCPM) | 5 | 0.957 | 89.12 | 0.006 | 0.904 | 74.06 | 0.009 |

flakes were compared on the basis of figures of merit (Tables III and V). The performances of the calibration models were found to improve with underside spectral acquisition irrespective of preprocessing methods for all three NIR

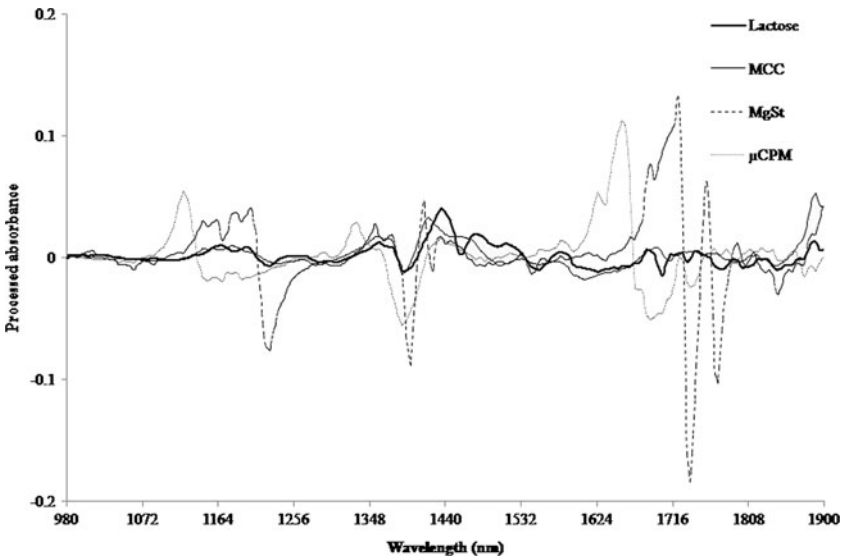


**Fig. 6.** SNV followed by first derivative preprocessed NIR reflectance spectra of flake components in powder form

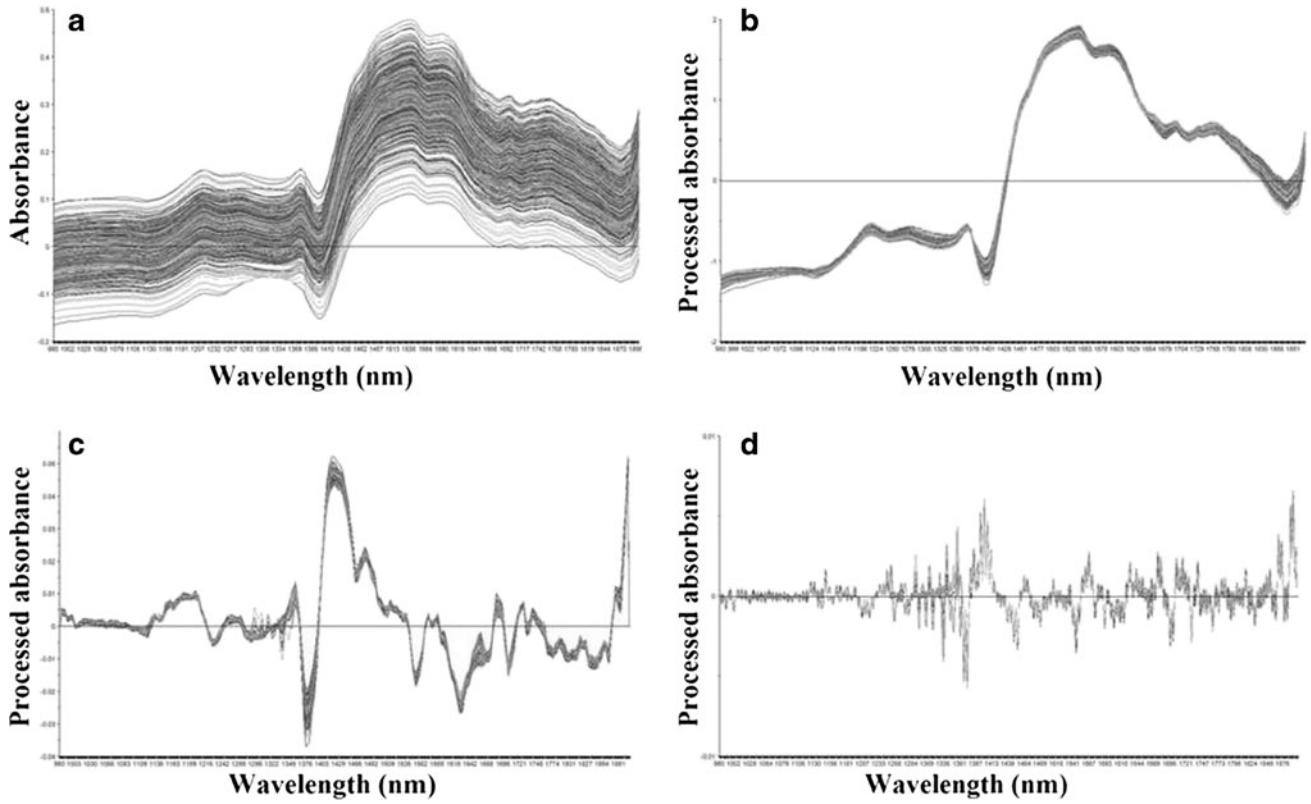


**Fig. 7.** NIR reflection spectra of calibration batch captured from the upper side of the flakes using QR 400 NIR probe. **a** Raw, **b** SNV, **c** SNV followed by first derivative, and **d** SNV followed by second derivative preprocessed

probes. The RMSEC and RMSEP values were reduced for all the models, with underside spectral acquisition strategy employing less or same number of PCs. Moreover, *X* and *Y* explained variances with models were comparable for both spectral acquisition strategies. By the upper side spectral acquisition, the constant gap between the flake surface and the probe could not be maintained for all the batches due to the differences in flake thickness. Flake thickness was found to increase with higher μCPM content and RF (Fig. 8). This observation could be attributed to higher feed rate at high RF and higher relaxation of flakes at high RF as μCPM is less compressible; higher concentrations of μCPM also resulted in thicker flakes. In addition, it was also found that the serrations on the flake surface tended to break at higher RF and this led to a decrease in the flake thickness. As a consequence, the slopes of the curves in Fig. 8 were found to show decreased

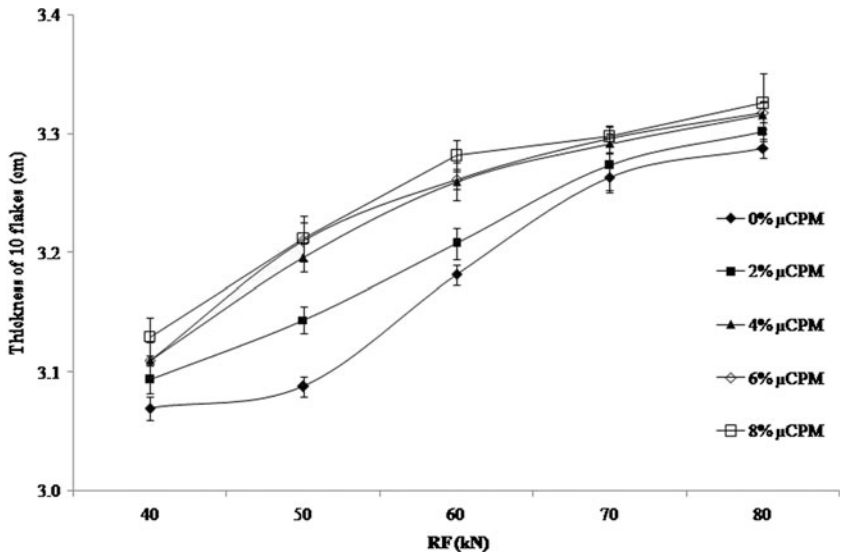


**Fig. 8.** Thickness of 10 flakes (in centimeters) at different μCPM concentrations and RF

trends at higher RF. Using the underside spectral acquisition, the variations in flake thickness did not adversely affect the specified gap between the flake surface and the probe. This gap was always maintained at a steady value as the flakes were always flat on the two parallel conveyor belts due to gravitational force and these belts were supported by a platform. Therefore, the improved performance with the underside spectral acquisition model could be attributed to the ability of the process to maintain the gap between the flake surface and the probe within a narrower range.

### Effect of Probe Diameter (Spot Size) on Calibration Model

Three NIR diffuse reflectance measurement probes, QR 200, QR 400, and QR 600 with the beam sizes of 0.6, 1.2, and 1.8 mm, respectively, were used for this study. The calibration models of these three probes built from SNV followed by first derivative preprocessed dynamic spectra were compared in terms of figures of merit (Table III). The lowest RMSEC, RMSEP, and number of PC were found with the QR 400 calibration models for all the models using both sampling strategies (upper side or underside). Between QR 200 and QR 600 probes, μCPM content was better modeled using the QR 600 probe, whereas TS, *E*, and RD were better modeled using the QR 200 probe. These probes were further compared on the basis of the prediction results using test set samples for known μCPM concentrations (Table VI). The lower standard deviation (SD) values were found for QR 400 probe and higher values were found for QR 200 for all the μCPM predicted concentrations. The lower SD values with QR 400 compared to QR 200 suggested that the QR 400 may be capturing appreciable variations in a single scan compared to QR 200 probe due to larger beam size. Interestingly, the lowest SD as attributed to strong averaging effect was not for the QR 600 probe despite having largest beam size. This could be due to acquisition of less stable spectra with small changes in the position of probe, specifically between the wavelength region of 1,200 and 1,400 nm. The QR 600 probe had also to be kept closer to the flake surface as compared with the other two probes for capturing relatively good quality spectra. Increasing the gap between QR 600 probe and flake surface led to the poorer quality spectra captured. Therefore, minor distortions on the flake surface and differences in flake surface profile, which were common in ribbed flakes, could not be as well compensated for the QR 600 probe, leading to higher SD values. Hence, overall, the QR 400 probe was the best and was selected for NIR spectra capture in the real-time roller compaction study.

Among the models, the μCPM concentration model showed the best results in terms of the number of PCs used and explained variances and residual errors at calibration and validation stages. This could be attributed to the uniform distribution of μCPM and strong spectral quality of μCPM throughout the blend during mixing of the blend components, especially during premixing of μCPM and lactose in high shear mixer. On the other hand, the relatively inferior models found with other flake attributes may be due to the larger variabilities in flake physical quality attributes, such as Young's modulus and RD. These later attributes also gave comparatively weaker spectral fingerprints.

**Table VI.** SDs of Prediction Results from the Test Set Sample for NIR Spectra Collected from the Underside of the Flakes

| | μCPM concentration (%, *w*/*w*), SD | | | | |
|---|---|---|---|---|---|
| Probe | 0 | 2 | 4 | 6 | 8 |
| QR 200 | 0.41 | 0.35 | 0.45 | 0.94 | 0.99 |
| QR 400 | 0.25 | 0.25 | 0.26 | 0.23 | 0.27 |
| QR 600 | 0.19 | 0.24 | 0.35 | 0.86 | 0.79 |

**Table VII.** Validation Results Obtained with Test Set for μCPM Content and CQA (Containing 4%, w/w μCPM) of Flakes

| Statistics | μCPM | TS | *E* | RD |
|---|---|---|---|---|
| Samples | 25 | 5 | 5 | 5 |
| No. of PC | 2 | 4 | 4 | 4 |
| Slope | 1.004 | 0.883 | 0.928 | 0.968 |
| Offset | −0.021 | 0.089 | 0.738 | 0.029 |
| Correlation | 0.997 | 0.982 | 0.971 | 0.983 |
| $R^2$ | 0.994 | 0.949 | 0.939 | 0.966 |
| RMSEP | 0.224 | 0.069 | 0.904 | 0.006 |
| Bias | −0.006 | −0.028 | −0.243 | 0.001 |
| SD of residual | 0.224 | 0.064 | 0.881 | 0.006 |

### Selection of Best Calibration Models for Real-Time Analysis

Sampling mode, spectral preprocessing method, probe position, and beam size collectively played respective roles in building the best calibration models for μCPM concentration, TS, *E*, and RD of ribbed flakes off-line. From the above findings, the dynamic mode of spectral acquisition from the underside of the flakes using QR 400 probe and SNV followed by first derivative spectral pretreatment were found to be optimal for building the best calibration models. The efficiencies of the best calibration models were confirmed by the TSV results (Table VII). All the models were found to exhibit linearity within the span of calibration and validation ranges as confirmed from the $R^2$ values. Accuracy of the models developed was estimated based on RMSEP and bias values obtained from TSV. Results obtained for RMSEP and bias values confirmed the accuracy of the models for predicting the μCPM and other properties of flakes containing 4%, *w*/*w* μCPM. Further estimates of accuracy for μCPM content, TS, *E*, and RD were given by the SDs of the residuals obtained after the TSV (Table VII).

### System Performance of Real-Time Application

Results obtained from the initial calibration and validation studies confirmed the accuracy of the developed models to predict the μCPM concentration, TS, *E*, and RD of the flakes. However, the next objective was to apply the developed models for their application in real-time monitoring during the roller compaction process. Considering the differences between the spectral acquisition in the calibration stage using a conveyor belt and the production stage using a rectangular channel, the occurrence of spectral difference was apprehended. These spectral differences could have negative effect on cross-correlation studies and may lead to erroneous

predictions. Hence, it was imperative to standardize the measured spectra in order to minimize the incorporation of process-borne effects during predictions. A possible treatment to minimize such differences was to standardize the flake movement's speed and spectral acquisition times during the calibration and production stages and to pretreat the spectra with suitable preprocessing techniques which had been shown to be able to minimize such effects. Equivalent linear speed of conveyor belt as RS, a fixed integration time of 100 ms for spectral acquisition, and different pretreatments were adopted at the calibration and production stages of analyses.

### Real-Time Analysis of Flakes

The best calibration models were uploaded into the Process Explorer using the OLUP to predict the μCPM content, TS, *E*, and RD from the real-time spectral data collected during roller compaction. Good agreement was obtained between the NIR predicted and the reference values for all flake attributes. Lesser variation was observed in the NIR-PLS1-predicted values for μCPM concentration (Fig. 9a) compared to the NIR-PLS1-predicted values for TS (Fig. 9b), *E* (Fig. 9c), and RD (Fig. 9d) of the flakes. Variations between these off-line and real-time spectral data could be attributed to the effect of 3 days relaxation time and temperature effect (15).

There was no time provided between analysis of sequential powder blends when analyzed dynamically which caused gradual increase of NIR-PLS1-predicted values at the time points of 2, 4, 6, and 8 min (Fig. 9a). Mixing of two consecutive powder blends occurred between two consecutive blends to some extent, which was reflected in 2, 4, 6, and 8 min of Fig. 9a. These results concur with the findings reported by Gupta *et al*. for the smooth roller-compacted flakes (16). In addition, it was also observed that, at time points of 2, 4, 6, and 8 min, NIR-PLS1-predicted RD, TS, and *E* values rose to higher values and decreased thereafter to steady-state levels. These were the time points when the RF values shifted to higher values. When RF was changed, vertical feeding screw speed was momentarily increased and then decreased by the automatic feedback system to reflect the higher RF value. This observation was also detected by the NIR spectra that were predicting the flakes attributes.

This good agreement between the NIR predicted and reference values in real-time for flakes despite the undulated surfaces could be attributed to the almost complete simulation of the situation during NIR real-time monitoring in off-line monitoring setup. Selection of suitable spectral preprocessing methods and suitable fiber optic probe diameter also helped to build the best NIR-PLS1 calibration model in determining the key flake attributes from the real-time spectral data.

A continuous but small amount of powder always leaked along the side seals during roller compaction. This resulted in the deposition of fine dust on the probe and fouling spectral acquisition. A previous study had shown that dust particles

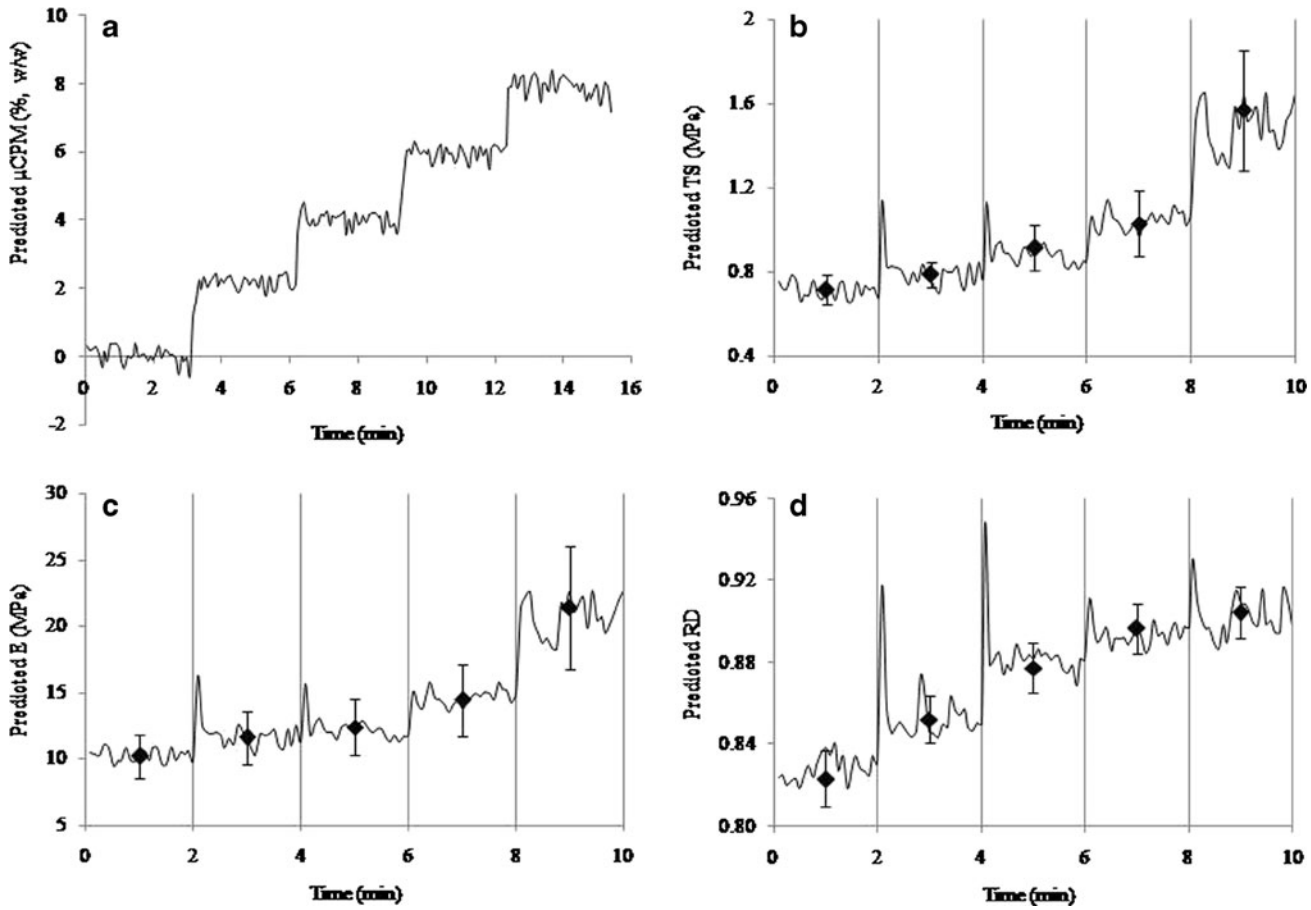


**Fig. 9.** PLS1-predicted values of **a** μCPM concentration, **b** TS, **c** *E*, and **d** RD from the NIR data collected during real-time monitoring of roller compaction (*diamonds* values determined using the reference method)

affected the NIR-predicted values by causing additional scatter of NIR signal (16). However, for the present study, these dust particles were removed from the spectral acquisition region by vacuuming the cover at the top of the rectangular channel. The strategy of vacuuming out of dust particles was found to be very effective. The lighter and finer dust particles with higher probability of deposition on the NIR probe were mainly removed by the vacuum. On the other hand, comparatively heavier and coarser dust particle had more chances of escaping the vacuuming region, but they were less likely to create a problem by depositing on the NIR probe. Real-time analysis was carried out for a maximum of 30 min at constant RF using a fixed powder blend and no marked effect in NIR signal was observed. Moreover, running of our industrial-scale roller compactor for several hours was out of scope as it required a lot of material. Only a small variation was observed in the NIR-PLS1-predicted values from both real-time and TSV data. Hence, it can be concluded that the NIR signal was not markedly affected.

### Continuous Quality Monitoring of the Roller Compaction Process

The experimental setup discussed in this study aimed at fulfilling the PAT goals of continuous quality monitoring of the process. As demonstrated, the present real-time monitoring study may be used to identify any substandard quality flakes, such as flakes containing higher or lower percentage of API and the overcompressed or undercompressed flakes in real time. The lower-quality flakes, if not detected earlier, may eventually affect the final product quality. Therefore, quality changes may be detected in-process and flakes that do not meet specifications can be separated out in real time. The feedback system of the roller compaction process can enable readjustment of the production conditions to ensure that only flakes within specifications are collected, hence affecting the final product quality.

## CONCLUSION

This study has demonstrated the successful application of NIR diffuse reflectance spectroscopy for monitoring of content uniformity and CQA of ribbed flakes with a high degree of accuracy during roller compaction. Due to the undulation of the flakes, maximum possible variability encountered during roller compaction was included during off-line calibration model development stages to build the more sensitive calibration models. In addition, flakes were manufactured with a wide range of μCPM concentration and RF to ensure robustness of the calibration models. The results suggested that dynamic spectral acquisition mode and appropriate probe positioning were very crucial in improving calibration model sensitivity. Spectra acquisition in dynamic mode minimized the variability that resulted from the flake's undulation. On the other hand, appropriate probe position maintained a constant gap between the flake surface and the probe head during spectral acquisition. Calibration model sensitivity was further improved by selecting a suitable spectral preprocessing method. In addition, the NIR diffuse reflectance probe used for real-time monitoring of content uniformity and properties of flakes can be made more effective by the selection of an appropriate beam size of fiber optic probe. Adequacy of models for real-time determination of μCPM concentration and other flake attributes was visible from RMSEP and TSV results. Finally, the best calibration models used in real-time to predict the μCPM concentration, TS, *E*, and RD of flakes, showed the smallest degree of variation in the results. Therefore, with the proposed setup, simultaneous determination of content uniformity and properties from ribbed roller-compacted flakes in a rapid, efficient, and nondestructive manner could be achieved.

## ACKNOWLEDGMENTS

The authors would like to acknowledge the financial support from GEA-NUS PPRL fund (N-148-000-008-001) and A*STAR SERC grant no. 102 161 0049 (R-148-000-157-305). The authors wish to thank Camo Software for the gratis supply of license for Unscrambler X and OLUP softwares; Carl Zeiss for loaning the NIR spectrophotometer; and GEA Pharma Systems for providing the IBC bin blender for this study.

## REFERENCES

1. Miller RW. Roller compaction technology. In: Parikh DM, editor. Handbook of pharmaceutical granulation technology. New York: Marcel Dekker; 1997. p. 99–150.
2. Miller RW, Sheskey PJ. Roller compaction technology for the pharmaceutical industry. In: Swarbrick J, editor. Encyclopedia of pharmaceutical technology. New York: Informa Healthcare USA; 2007. p. 3159–76.
3. Daugherity PD, Chu JH. Investigation of serrated roll surface differences on ribbon thickness during roller compaction. Pharm Dev Technol. 2007;12(6):603–8.
4. Dec RT, Zavaliangos A, Cunningham JC. Comparison of various modeling methods for analysis of powder compaction in roller press. Powder Technol. 2003;130(1–3):265–71.
5. Turkoglu M, Aydin I, Murray M, Sakr A. Modeling of a roller-compaction process using neural networks and genetic algorithms. Eur J Pharm Biopharm. 1999;48(3):239–45.
6. Johanson JR. A rolling theory of granular solids. J Appl Mech. 1965;32(4):842–8.
7. Bacher C, Olsen PM, Bertelsen P, Kristensen J, Sonnergaard JM. Improving the compaction properties of roller compacted calcium carbonate. Int J Pharm. 2007;342(1–2):115–23.
8. Bacher C, Olsen PM, Bertelsen P, Sonnergaard JM. Granule fraction inhomogeneity of calcium carbonate/sorbitol in roller compacted granules. Int J Pharm. 2008;349(1–2):19–23.
9. Ghorab MK, Chatlapalli R, Hasan S, Nagi A. Application of thermal effusivity as a process analytical technology tool for monitoring and control of the roller compaction process. AAPS Pharm Sci Tech. 2007;8(1):23.
10. Department of Health and Human Services, US Food and Drug Administration. Pharmaceutical CGMPs for the 21st century—a risk-based approach: final report. http://www.fda.gov/downloads/Drugs/DevelopmentApprovalProcess/Manufacturing/QuestionsandAnswersonCurrentGoodManufacturingPracticescGMPforDrugs/UCM176374.pdf (2004).
11. US Food and Drug Administration. Guidance for industry, PAT—a framework for innovative pharmaceutical development, manufacturing and quality assurance. http://www.fda.gov/downloads/Drugs/GuidanceComplianceRegulatoryInformation/Guidances/ucm070305.pdf (2004).
12. Hakanen A, Laine E. Acoustic characterization of a microcrystalline cellulose powder during and after its compression. Drug Dev Ind Pharm. 1995;21(13):1573–82.
13. Hakanen A, Laine E, Jalonen H, Linsaari K, Jokinen J. Acoustic emission during powder compaction and its frequency spectral analysis. Drug Dev Ind Pharm. 1993;19(19):2539–60.

14. Salonen J, Salmi K, Hakanen A, Laine E, Linsaari K. Monitoring the acoustic activity of a pharmaceutical powder during roller compaction. Int J Pharm. 1997;153(2):257–61.
15. Feng T, Wang F, Pinal R, Wassgren C, Carvajal MT. Investigation of the variability of NIR in-line monitoring of roller compaction process by using fast Fourier transform (FFT) analysis. AAPS Pharm Sci Tech. 2008;9(2):419–24.
16. Gupta A, Peck GE, Miller RW, Morris KR. Real-time near-infrared monitoring of content uniformity, moisture content, compact density/tensile strength, and Young's modulus of roller compacted powder blends. J Pharm Sci. 2005;94 (7):1589–97.
17. Miller RW. Roller compaction optimization—NIR in-process mapping. Pharmaceutical Technology Europe. 2000;12(4):48–55.
18. Gupta A, Peck GE, Miller RW, Morris KR. Nondestructive measurements of the compact strength and the particle-size distribution after milling of roller compacted powders by near-infrared spectroscopy. J Pharm Sci. 2004;93(4):1047–53.
19. Cogdill RP, Anderson CA, Delgado-Lopez M, Molseed D, Chisholm R, Bolton R, *et al*. Process analytical technology case study part I: feasibility studies for quantitative near-infrared method development. AAPS Pharm Sci Tech. 2005;6(2):E262–72.
20. Akseli I, Iyer S, Lee HP, Cuitiño AM. A quantitative correlation of the effect of density distributions in roller-compacted ribbons on the mechanical properties of tablets using ultrasonics and X-ray tomography. AAPS PharmSciTech. 2011;12(3):834–53.
21. Gamble JF, Tobyn M, Dennis AB, Shah T. Roller compaction: application of an in-gap ribbon porosity calculation for the optimization of downstream granule flow and compactability characteristics. Pharm Dev Technol. 2010;15(3):223–9.
22. Soh JLP, Boersen N, Carvajal MT, Morris KR, Peck GE, Pinal R. Importance of raw material attributes for modeling ribbon and granule properties in roller compaction: multivariate analysis on roll gap and NIR spectral slope as process critical control parameters. J Pharm Innov. 2007;2(3–4):106–24.
23. Soh JLP, Wang F, Boersen N, Pinal R, Peck GE, Carvajal MT, *et al*. Utility of multivariate analysis in modeling the effects of raw material properties and operating parameters on granule and ribbon properties prepared in roller compaction. Drug Dev Ind Pharm. 2008;34(10):1022–35.
24. Lim H, Dave VS, Kidder L, Neil Lewis E, Fahmy R, Hoag SW. Assessment of the critical factors affecting the porosity of roller compacted ribbons and the feasibility of using NIR chemical imaging to evaluate the porosity distribution. Int J Pharm. 2011;410(1–2):1–8.
25. Esbensen KH. Multivariate data analysis—in practice. Oslo: CAMO Process AS; 2004.
26. Li T, Donner AD, Choi CY, Frunzi GP, Morris KR. A statistical support for using spectroscopic methods to validate the content uniformity of solid dosage forms. J Pharm Sci. 2003;92(7):1526–30.
27. Gupta A, Peck GE, Miller RW, Morris KR. Influence of ambient moisture on the compaction behavior of microcrystalline cellulose powder undergoing uni-axial compression and roller-compaction: a comparative study using near-infrared spectroscopy. J Pharm Sci. 2005;94(10):2301–13.
28. Gupta A, Peck GE, Miller RW, Morris KR. Effect of the variation in the ambient moisture on the compaction behavior of powder undergoing roller-compaction and on the characteristics of tablets produced from the post-milled granules. J Pharm Sci. 2005;94(10):2314–26.
29. Beebe R, Pell RJ, Seasholtz MB. Multivariate calibration and prediction. Chemometrics: a practical guide. New York: Wiley; 1998. p. 280.
30. Honigs DE. Three constant themes in NIR analysis. In: Hildrum KI, Isaksson T, Naes T, Tandberg A, editors. Near infra-red spectroscopy: bridging the gap between data analysis and NIR applications. Sussex: Ellis Harwood Ltd.; 1992. p. 109–18.
31. Blanco M, Coello J, Iturriaga H, Maspoch S, De La Pezuela C. Effect of data preprocessing methods in near-infrared diffuse reflectance spectroscopy for the determination of the active compound in a pharmaceutical preparation. Appl Spectrosc. 1997;51 (2):240–6.
32. Olinger JM, Griffiths PR. Effects of sample dilution and particle-size morphology on diffuse reflection spectra of carbohydrate systems in the near-infrared and midinfrared.1. Single analytes. Appl Spectrosc. 1993;47(6):687–94.
33. Olinger JM, Griffiths PR. Effects of sample dilution and particle-size morphology on diffuse reflection spectra of carbohydrate systems in the near-infrared and mid-infrared.2. Durum-wheat. Appl Spectrosc. 1993;47(6):695–701.